Bubble and pattern formation in liquid induced by an electron beam – Supporting Information

Joseph M. Grogan[a,†], *Nicholas M. Schneider*[a], *Frances M. Ross*[b,+], *and Haim H. Bau*[a,*]

[a]Department of Mechanical Engineering and Applied Mechanics, the University of Pennsylvania, Philadelphia, PA 19104, USA.

[b]IBM T. J. Watson Research Center, Yorktown Heights, NY 10598, USA.

† Now at Hummingbird Scientific, Lacey, WA 98516, USA.

*bau@seas.upenn.edu

[+]fmross@us.ibm.com

Video observations and analysis of bubble formation and growth

Supplementary Video 1 features three examples of nanoscale bubbles observed in an aqueous solution of gold nanorods (pH ~ 7) with trace amounts of the surfactant cetrimonium bromide (CTAB). Imaging was performed with a Hitachi 9000 TEM (300 keV) at beam current $I < 1$ nA and beam radius $a \sim 2$ μm.

Supplementary Video 2 features an example of a large "explosive" bubble observed in an aqueous solution of 20 mM $HAuCl_4$ (pH < 2). Imaging was performed with a FEI Quanta 600 in

STEM mode (30 keV) at beam currents of $I = 0.05 - 1.2$ nA, beam radius $a \sim 0.5 - 1.5$ nm, and raster area of $\sim 1\ \mu m^2$. The bubble formed after nearly an hour of observing nanoparticle growth. Prior to bubble formation, the sample was moved around frequently to image various parts of the window for tens of seconds to a few minutes at any location.

Supplementary Video 3 features another large bubble in the same device that produced Supplementary Video 2. After forming the bubble in Supplementary Video 2, the device remained sealed for several days. On further imaging, the bubble was absent, presumably redissolved, but after about 1 minute of imaging, another large bubble appeared and grew at a rate dependent on the beam current. The slowdown in growth is visible as the bubble occupied more of the membrane window.

Estimates of Beam-Induced Heating

Here we show that beam-induced temperature rise is insignificant under typical (S)TEM imaging conditions. Our approach allows us to consider a wider range of operating conditions (*i.e.*, the beam energy, current, and geometry) than previous analysis,[S1] and is also more precise in calculating the energy transfer per incident electron.

We use the ESTAR database for electron stopping power (S) available from NIST.[S2] When tabulated values are not available, the Bethe formula can be used to estimate the stopping power.[S3] Over the range of incident energies relevant to electron microscopy, stopping power decreases with increasing electron energy. For a particular incident electron, we take S to be a constant throughout the interaction. This assumption is valid when the sample thickness does not exceed a few times the electron mean free path λ, allowing us to approximate the incident electron path length by the liquid height. This condition is reasonable for most typical liquid

cells, for which $h_{\mathrm{liq}} \leq 1\ \mu\mathrm{m}$ while the mean free path of 30keV – 300keV electrons in water $\lambda =$ 10s to 100s of nm.[S4] Note that if $h_{\mathrm{liq}} \gg \lambda$, most of the energy will be absorbed by the medium and one would employ, with moderate accuracy, the continuous slowing down approximation (CSDA).[S3] The membranes are also thin (*i.e.*, the path length through each membrane $\sim h_{\mathrm{SiN}}$).

The volumetric rate of energy deposited in the sample through inelastic collisions (in $\mathrm{W/m^3}$) is:

$$q = \frac{S\ \rho\ 10^8\ I}{\pi\ a^2}, \tag{S 1}$$

where S is the density-normalized stopping power $(\mathrm{MeV\ cm^2/g\ electron})$, ρ is the density $(\mathrm{g/cm^3})$, I is the current $(\mathrm{C/s})$, a is the radius of the beam (m), and 10^8 $(\mathrm{cm\ electron\ J/m\ MeV\ C})$ accounts for unit conversions.

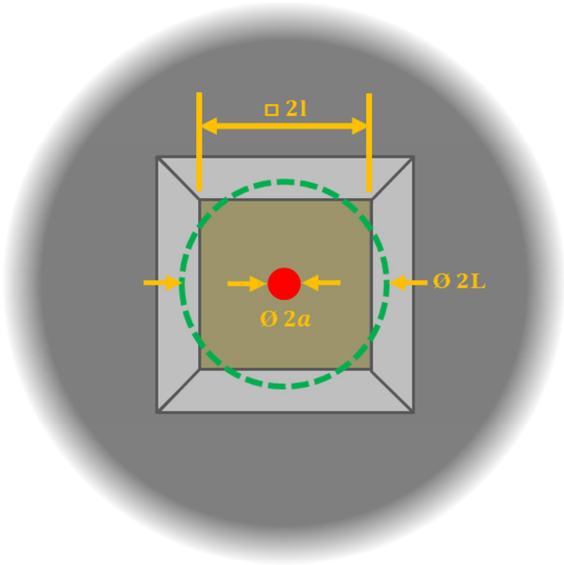

Supplementary Figure 1. Top view of the imaging window depicting the square silicon nitride membrane window ($2l = 100$ μm). The beam (red disk) radius is a. The outer boundary of the computational domain (dashed green circle with diameter $2L$) has the same area as the actual window. The bulk Si material surrounding the window region is shown in gray.

The intersection of the beam with the imaged medium forms a cylindrical volume with radius a that is subject to uniform heat generation q (equation (S 1)). We consider the case when the beam is located at the center of the window (Supplementary Figure 1) as this will result in the maximum temperature increase. Even for a large temperature rise (*e.g.*, 100 ℃), heat transfer in the system is dominated by conduction and we can neglect radiation. Furthermore, we assume that the surfaces in contact with the vacuum environment of the microscope are insulating and that there are no significant temperature variations in the vertical direction. For simplicity, we model the heat transfer as a one-dimensional cylindrical problem and approximate the window geometry (edge length of $2l$) with a disk of diameter of $2L$ that has the same area as the actual window (*i.e.*, $L = 2\,l/\sqrt{\pi}$). The silicon body of the liquid cell acts as an effective heat sink due to the high thermal conductivity of the silicon, its relatively large size compared to that of the window region, and its contact with the sample holder. Thus, we assume that the silicon body is at the ambient temperature (T_0 at $r = L$) at all times.

We solve the dimensionless heat equation:

$$\frac{\partial \tilde{\theta}}{\partial \tilde{t}} - \tilde{\nabla}^2 \tilde{\theta} = 1 \qquad \text{(inside the beam, } 0 \le \tilde{r} \le 1\text{)} \tag{S 2}$$

$$\frac{\partial \tilde{\theta}}{\partial \tilde{t}} - \tilde{\nabla}^2 \tilde{\theta} = 0 \qquad \text{(outside the beam, } 1 < \tilde{r}\text{)}. \tag{S 3}$$

We adopt the convention that quantities with a wiggle are dimensionless while plain letters represent dimensional quantities. In the above, length is normalized by the beam radius a and time is normalized by the diffusive time a^2/α_{th}, where α_{th} is the thermal diffusivity. Temperature rise $(T - T_0)$ in ℃ is normalized by $a^2 q\, 10^{-6}/\left(\alpha_{\text{th}}\, C_p\, \rho\right)$ to get dimensionless temperature rise $\tilde{\theta}$, where C_p is the specific heat at constant pressure, and 10^{-6} (m^3/cm^3)

accounts for unit conversions to express ρ in $\mathrm{g/cm^3}$ as is common in radiation chemistry. The boundary and initial conditions include symmetry about the origin ($r = 0$), ambient temperature at the outer boundary $\tilde{\theta}(\tilde{L}, \tilde{t}) = 0$, where $\tilde{L} = L/a$, and initial temperature $\tilde{\theta}(\tilde{r}, 0) = 0$. The maximum temperature is achieved at steady-state ($\tilde{t} \to \infty$), when the temperature distribution is

$$\tilde{\theta}_{\mathrm{SS}}(\tilde{r}) = \begin{matrix} \frac{1}{4}(1-\tilde{r}^2) + \frac{1}{2}\mathrm{Ln}[\tilde{L}] & (\,0 \le \tilde{r} \le 1) \\ \frac{1}{2}\mathrm{Ln}\left[\frac{\tilde{L}}{\tilde{r}}\right] & (1 < \tilde{r} \le \tilde{L}) \end{matrix}. \quad \text{(S 4)}$$

The maximum temperature rise (in dimensional form) is at the center of the beam:

$$\Delta T_{\max} = \frac{S\, I\, 10^2}{\pi\, \alpha_{\mathrm{th}}\, C_p}\left(\frac{1}{4} + \frac{1}{2}\mathrm{Ln}\left[\frac{L}{a}\right]\right), \quad \text{(S 5)}$$

where 10^2 $(\mathrm{m^2\ electron\ J/cm^2\ MeV\ C})$ accounts for unit conversions. The temperature maximum is a linear function of beam current I and independent of the layer's thickness.

Supplementary Figure 2 depicts contours of temperature rise in the water layer as a function of beam current I and beam radius a when the acceleration voltage is 300 keV (left) and 30 keV (right). $L = \frac{2}{\sqrt{\pi}}\ 50 \times 10^{-6}$ m, $\alpha_{\mathrm{th\ water}} = 1.4 \times 10^{-7}\ \mathrm{m^2/s}$,[S5] and $C_{p\ \mathrm{water}} = 4.18\ \mathrm{J/g\ K}$.[S6] In most of our imaging experiments, TEM beam current is ≤ 10 nA and STEM beam current is ≤ 1 nA, which would result in a maximum temperature rise of less than 4 ℃.

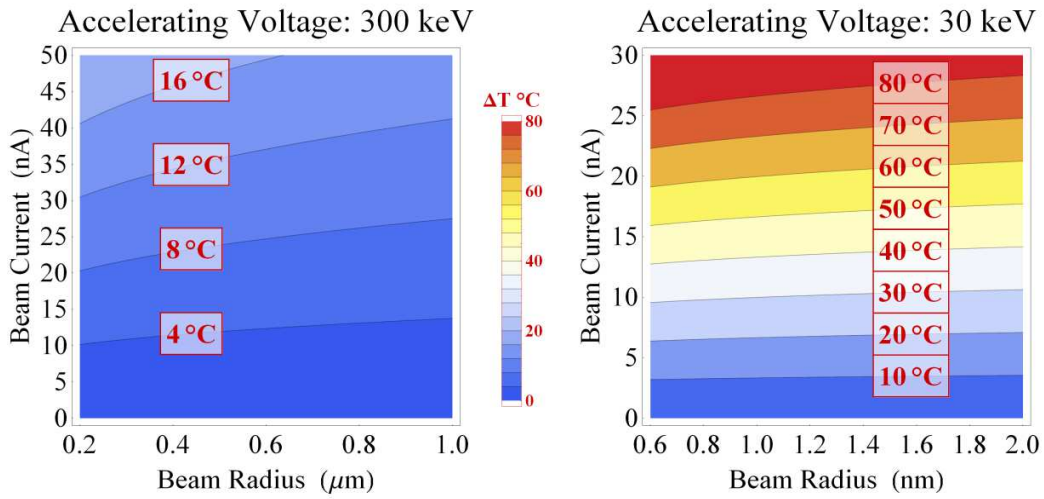

Supplementary Figure 2. Contours of estimated temperature rise in a water layer as functions of beam radius and beam current due to electron beam-induced heating typical to TEM (left) and lower-keV STEM (right). The boxed numbers label the temperature rise contours.

Equation (S 5) predicts that the temperature rise in the silicon nitride membrane differs from that in the water by the material-dependent term: $S/\alpha_{\text{th}}\, C_p$. With $\alpha_{\text{SiN}} = 1.12 \times 10^{-5} - 2.10 \times 10^{-5}$ m^2/s,[S7] and $C_{p\,\text{SiN}} = 0.54 - 0.70$ J/g K,[S7] we find that the temperature rise is $16 - 24$ times lower than in water, and may be ignored. Additionally, the temperature rise plotted in Supplementary Figure 2 is likely an overestimation because it neglects heat transfer from the water layer to the silicon nitride membrane, which has a thermal conductivity that is almost an order of magnitude greater than that of water ($k_{\text{water}} = 0.59$ W/m K,[S5] $k_{\text{SiN}} = 25 - 36$ W/m K[S7]).

Water radiolysis by electrons and other high energy species

The chain of events induced by any ionizing radiation is generally the same regardless of the nature of the radiation, *i.e.*, visible light, UV light, X-rays, γ-rays, neutrons, α-particles (helium),

electrons, and positrons.[S3] Molecules are excited and ionized by the radiation and the resulting radicals, ions, molecular species, and freed electrons react chemically to yield byproducts.

A complex chain of events takes place during radiolysis. Immediately after the moment of energy transfer, a cluster of byproducts is formed in an entity called a spur. Spurs are spaced, on average, by the electrons' mean free path.[S3] The amount of each species (the yield) produced $(+)$ or destroyed $(-)$ per 100 eV absorption from ionizing radiation is quantified empirically through the G-value (Supplementary Table 1). The short-time yield, denoted $g(X)$ or $G^0(X)$ and referred to as the primary yield or initial yield, describes the species that are produced within the spur immediately after the energy transfer event. Kinetics at short times (< 1 μs) can be described by a few reactions, as employed in spur models. After the spur dies out, surviving byproducts diffuse freely and continue to react further. The long-time yield, denoted $G(X)$ or $G_{\mathrm{esc}}(X)$ and referred to as the homogeneous yield, steady-state yield, escape yield, or observed yield, describes the species that made it out of the spur and exist 1 μs after the energy transfer event, at which point the spur has relaxed (achieved locally uniform concentration). The long-time kinetics (> 1 μs) require all reaction pathways to be considered, resulting in kinetic models with upwards of ~ 80 reactions for neat water,[S8] and more when additional species are present.

$G(X)$ and $g(X)$ can differ. For example, in methanol radiolysis, $\mathrm{H_2}$ is produced in the spur directly, but it is also produced indirectly by the reaction $\mathrm{H + CH_3OH \rightarrow H_2 + CH_2OH}$. So the observed yield of $\mathrm{H_2}$ comes from two sources, $G(\mathrm{H_2}) \propto g(\mathrm{H_2}) + g(\mathrm{H})$. By performing experiments in the presence of different scavengers, the various $G(X)$ and $g(X)$ values can be teased apart.[S3] When forming a diffusion-kinetic model of a system beyond a single spur, $G(X)$ is used to describe the production rate of species X. To assess the impact of scavenger solutes on

$G(X)$, one needs to solve the diffusion-reaction equations in the spur using the primary yield $g(X)$ and account for reactions with the solute species.[S9]

Supplementary Table 1. G-value and diffusion coefficient for low-LET radiation in neat (pure) water.

Species	$G(X)\left(\frac{\text{molecules}}{100\text{ eV}}\right)$	D (m^2/s)	Source
e_h	2.7 ± 0.1	4.5×10^{-9}	S3,S9
H_3O^+	2.7 ± 0.1	9×10^{-9}	S3,S9
OH	2.7 ± 0.1	2.8×10^{-9}	S3,S9
H	0.56 ± 0.05	7×10^{-9}	S3,S9
H_2	0.44 ± 0.02	7×10^{-9}	S3,S9
H_2O_2	0.72 ± 0.02	2.2×10^{-9}	S3,S9
H_2O	-4.14	2.27×10^{-9}	S3,S10

Non-linear dose rate effects in STEM and TEM

Typically, the reported escape yield $G(X)$ for low-LET radiation assumes that the spurs are spaced out and do not interact. But as the dose-rate increases, more electrons pass through the sample and the number of energy transfer events increases, potentially leading to spur overlap. Spur overlap increases the likelihood that radicals will interact to yield molecular species, which for neat water include H_2, H_2O_2, and recombined H_2O.[S8] The effect of spur overlap can be inferred from intermediate and high-LET (linear energy transfer) systems in which the mean free path is short and energy loss occurs along a continuous track. For example, in neat water,

$G(\mathrm{H_2}) = 0.45$ for low-LET γ-rays (non-interacting spurs) while $G(\mathrm{H_2}) = 1.2$ for high-LET α-particles (tracks).[S8]

Spurs form along the electron path like beads on a string. Spurs are, on average, spaced out by the mean free path λ (Supplementary Figure 3). The concentrations of the radiolysis byproducts formed by the energy transfer event have a Gaussian spatial distribution with variance $\sigma_{\mathrm{spur}}{}^2$. The spur is approximated as a spherical volume with radius $r_{\mathrm{spur}} = \sigma_{\mathrm{spur}}/\sqrt{2}$.[S11] On average, the number of spurs produced by an electron moving through a medium in time t is given by

$$n_{\mathrm{spurs}} = \frac{h_{\mathrm{liq}}\, I\, t}{\lambda\, e}, \tag{S 6}$$

where h_{liq} is the sample thickness, λ is the electron mean free path, I is the beam current (in $\mathrm{C/s}$), and e is the electron charge $(\mathrm{C/electron})$. The average volume that contains a single spur is $\pi\, a^2\, \lambda\, e/I\, t$. Treating each volume as a sphere, we find that the average distance between adjacent spur centers is:

$$d_{\text{spur-spur, stationary}} = \left(\frac{6\, e\, \lambda\, a^2}{I\, t}\right)^{1/3}. \tag{S 7}$$

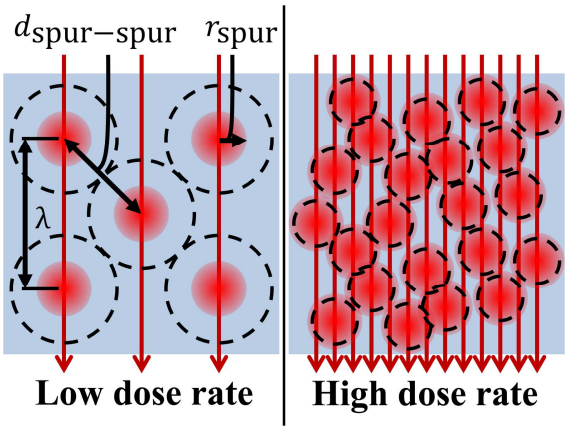

Supplementary Figure 3. Schematic illustration of spur formation when electrons pass through matter. Dark red lines represent the incident electron path. Bright red circles represent spurs. Spurs are dynamic;

once formed, they relax in about 1 μs. The illustration depicts a snapshot in time. The average distance between spurs in the snapshot can be determined by calculating the spherical volume that contains a single spur (dashed black lines). At high dose-rate irradiation we expect spurs to overlap. Spur overlap may modify the radiation chemistry of the system.

Since the STEM beam rasters, the irradiation and thus the spurs are spread out. The distance covered by the beam is given by the beam velocity v multiplied by time t. The volume swept out by the moving beam is $(\pi\, a^2 + 2\, a\, v\, t)\, h_{\mathrm{liq}}$. When $v\, t \gg a$, the volume can be approximated by $2\, a\, v\, t\, h_{\mathrm{liq}}$. Dividing this by the number of spurs (equation (S 6)), we find that the average distance between adjacent spherical spur centers is:

$$d_{\text{spur-spur, moving}} = \left(\frac{12\, e\, \lambda\, a\, v}{\pi\, I}\right)^{1/3}. \qquad \text{(S 8)}$$

We expect spurs to overlap when the distance between spurs is smaller than approximately $5\, \sigma_{\mathrm{spur}}$ (based on the Gaussian profile). σ_{spur} depends on the species under consideration. The smallest σ_{spur} value for most species in water radiolysis is $\sigma_{\mathrm{spur}} \sim 1.2$ nm.[S11] This yields the condition for spur overlap: $d_{\text{spur-spur}} \leq 6$ nm. Our time period of interest is the lifetime of a spur $t = 1$ μs.[S8] Supplementary Figure 4 depicts spur spacing for a stationary beam as a function of beam radius ((a) & (b)) and for a moving beam as a function of beam velocity ((c) & (d)) at various beam energies and currents. The dashed line indicates the onset of spur overlap.

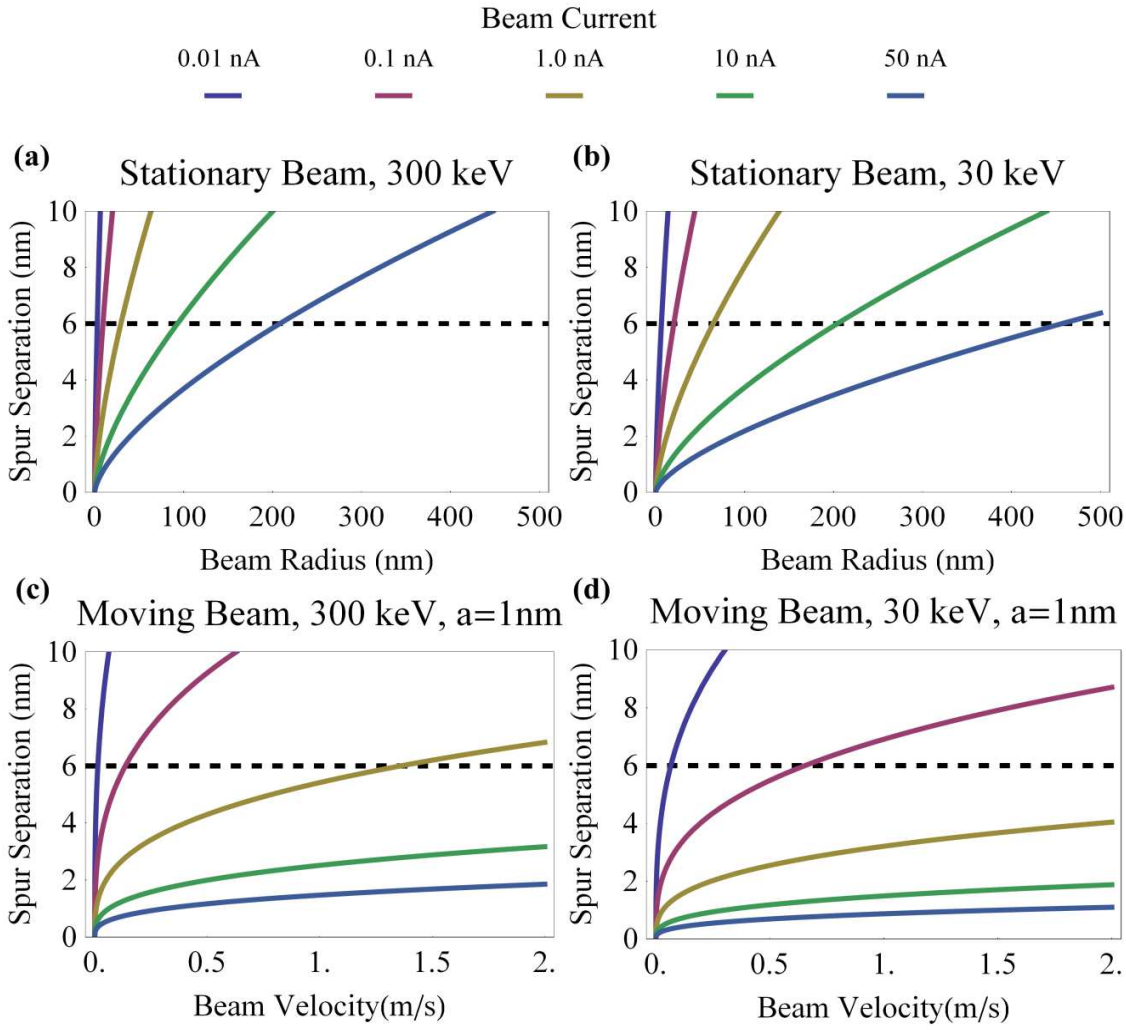

Supplementary Figure 4. Center-to-center spacing of spurs produced by high energy electrons in water. Results for a stationary beam as a function of beam radius are shown for 300 keV electrons (a) and 30 keV electrons (b). Results for a moving beam with radius $a = 1$ nm as a function of beam velocity are shown for 300 keV electrons (c) and 30 keV electrons (d). The criteria for spur overlap, $d_{\text{spur-spur}} \leq 6$ nm, is indicated with a black dashed line in each plot. Operating conditions with spur separation lower than this value should produce spur overlap.

Although there are conditions in the TEM that could produce spur overlap, such as a 300 keV beam with $I = 50$ nA and $a = 150$ nm, typical imaging at low to moderate dose-rates with a

spread beam should not produce spur overlap. However, when the beam radius a is reduced, as in STEM, the results are more extreme. A stationary STEM beam is certain to produce overlapping spurs. A moving STEM beam may or may not have spur overlap, depending on the operating conditions. Determining the velocity of the rastering beam is complicated because the beam spends some time moving from spot to spot and some time dwelling at a particular spot to acquire a pixel for the image. A few calculations of beam velocity for a FEI Quanta 600 rastering a $1024\ \text{pixel} \times 884\ \text{pixel}$ image with horizontal field width (HFW) of $10\ \mu\text{m}$ are shown in Supplementary Table 2.

Supplementary Table 2. STEM beam rastering properties for a $1024\ \text{pixel} \times 884\ \text{pixel}$ image with a horizontal field width $\text{HFW} = 10\ \mu\text{m}$

Dwell time (μs)	Frame Time (ms)	Mean Velocity (m/s)	No-Dwell Velocity (m/s)
3.00	2850	0.003	0.132
1.00	967	0.009	0.286
0.30	317	0.029	0.389
0.10	117	0.076	0.668
0.05	61.2	0.144	1.109

In Supplementary Table 2, the dwell time (and consequently the frame time) is selected by the user. We calculate the corresponding velocity two different ways. The mean velocity is calculated by dividing the HFW by the total time per line (frame time/884 lines) and does not distinguish between time spent dwelling and time spent moving. The no-dwell velocity is

calculated by multiplying the dwell time by the number of horizontal pixels (1024) and then subtracting the result from the time per line. This gives the time spent moving per line. We divide the HFW by half of this time, assuming that half of the time is spent moving from left to right and the other half is spent returning from right to left. This gives an upper bound on the beam velocity since the calculation ignores the time that the beam spends dwelling. If the no-dwell velocity is not fast enough to prevent spur overlap, then spurs will overlap. For example, the maximum no-dwell velocity for our microscope is $\sim 1.1\ \mathrm{m/s}$; therefore, from Supplementary Figure 4d we find that a $30\ \mathrm{keV}$ beam with $a = 1\ \mathrm{nm}$ and $I = 1\ \mathrm{nA}$ cannot possibly raster fast enough to prevent spur overlap.

Under typical imaging conditions, spur overlap is unlikely in the TEM but possible in the STEM. Depending on imaging conditions, altered chemical kinetics due to spur overlap should be considered for STEM, potentially changing concentrations by large amounts.

Reaction-Diffusion Model & Finite Element Modeling for $\mathrm{H_2}$

For the production rate of $\mathrm{H_2}$, we fit the dose-rate-dependent $\mathrm{H_2}$ data of Joseph *et al.*[S12] for γ-radiolysis at $2.5\ \mathrm{Gy/s}$ of deaerated water at pH 6; see main text. The result predicts that steady-state is approached asymptotically. To estimate the time needed to establish steady state in a uniformly irradiated sample, we arbitrarily define the system to be at steady-state when $C_{\mathrm{H_2}} = 0.99\, C_{\text{steady-}\mathrm{H_2}}$. For a uniformly irradiated sample, a dose-rate corresponding to $300\ \mathrm{keV}$ electrons, beam current $I = 10\ \mathrm{nA}$, and beam radius $a = 500\ \mathrm{nm}$ reaches steady-state in $\sim 0.01\ \mathrm{s}$; and a dose-rate corresponding to $300\ \mathrm{keV}$ electrons, beam current $I = 0.1\ \mathrm{nA}$, and beam radius $a = 2\ \mu\mathrm{m}$ reaches steady-state in $\sim 0.6\ \mathrm{s}$. In liquid cells where the fluid of interest

is encapsulated and uniformly irradiated (*e.g.*, encapsulation with graphene membranes[S13]), the steady-state will indeed be reached very quickly. In most liquid cell experiments, however, the sample is irradiated only over a small beam area. It will therefore take longer to reach steady-state in the liquid cell experiment because diffusion removes radiolysis byproducts from the irradiated volume.

To model the effect of diffusion on the concentration of species *X*, we solved the dimensionless reaction-diffusion equation using finite elements with the reaction rate Φ_X from equation (4):

$$\begin{aligned} &\frac{\partial \tilde{C}_X}{\partial \tilde{t}} - \tilde{\nabla}^2 \tilde{C} = \tilde{R}\left(1 - \frac{\tilde{C}_{\mathrm{X}}}{\tilde{C}_{\text{steady-X}}}\right)^2 \mathrm{H}\left(\tilde{C}_{\text{steady-X}} - \tilde{C}_{\mathrm{X}}\right) \qquad \text{inside the beam } (0 \le \tilde{r} \le 1) \\ &\frac{\partial \tilde{C}_{\mathrm{X}}}{\partial \tilde{t}} - \tilde{\nabla}^2 \tilde{C}_{\mathrm{X}} = -\frac{\tilde{C}_{\mathrm{X}}}{\tilde{\tau}_X} \qquad \text{outside the beam } (1 < \tilde{r}). \end{aligned} \tag{S 9}$$

In the above, length is normalized by the beam radius a, time is normalized by the diffusion time a^2/D, D is diffusivity, and τ_X is the relaxation time. $\mathrm{H}(x)$ is the Heaviside function ($\mathrm{H}(x < 0) = 0$ and $\mathrm{H}(x > 0) = 1$), which is included to prevent the concentration from growing uncontrollably if a numerical error yields $\tilde{C}_X > \tilde{C}_{\text{steady-}X}$. Also,

$$\tilde{R}_{\mathrm{X}} = \frac{a^2}{D} R_X = \frac{S\,\rho\,10^5\,I\,G(\mathrm{X})}{e\,\pi\,N_A\,D_X}. \tag{S 10}$$

Equation (S 9) was solved for the actual geometry of our liquid cell assuming impermeable boundary conditions around the computational domain (Figure 3a). To estimate the accumulation of H_2 in a pristine liquid cell, the results of which are depicted in Figure 3b and c, an initial uniform concentration of zero was imposed. The system still approaches steady state in a few seconds, relatively fast compared to the timescale of an experiment.

SUPPORTING INFORMATION REFERENCES

S1. Zheng, H.; Claridge, S. A.; Minor, A. M.; Alivisatos, A. P.; Dahmen, U. Nanocrystal Diffusion in a Liquid Thin Film Observed by in Situ Transmission Electron Microscopy. *Nano Letters* **2009**, *9*, 2460–2465.

S2. Berger, M. J.; Coursey, J. S.; Zucker, M. A.; Chang, J. NIST Stopping-Power and Range Tables: Electrons, Protons, Helium Ions http://www.nist.gov/pml/data/star/index.cfm/ (accessed Aug 14, 2012).

S3. Mozumder, A. *Fundamentals of Radiation Chemistry*; Academic Press, 1999.

S4. LaVerne, J. A.; Pimblott, S. M. Electron Energy-Loss Distributions in Solid, Dry DNA. *Radiation Research* **1995**, *141*, 208–215.

S5. James, D. W. The Thermal Diffusivity of Ice and Water Between- 40 and+ 60 C. *Journal of Materials Science* **1968**, *3*, 540–543.

S6. Cengel, Y. A.; Boles, M. A. *Thermodynamics: An Engineering Approach*; 3rd ed.; WCB/McGraw-Hill, 1998.

S7. Pierson, H. O. Handbook of Chemical Vapor Deposition (CVD) - Principles, Technology and Applications (2nd Edition) **1999**.

S8. Pastina, B.; LaVerne, J. A. Effect of Molecular Hydrogen on Hydrogen Peroxide in Water Radiolysis. *The Journal of Physical Chemistry A* **2001**, *105*, 9316–9322.

S9. LaVerne, J. A.; Pimblott, S. M. Scavenger and Time Dependences of Radicals and Molecular Products in the Electron Radiolysis of Water: Examination of Experiments and Models. *J. Phys. Chem.* **1991**, *95*, 3196–3206.

S10. Tanaka, K. Self-diffusion Coefficients of Water in Pure Water and in Aqueous Solutions of Several Electrolytes with 18O and 2H as Tracers. *J. Chem. Soc., Faraday Trans. 1* **1978**, *74*, 1879–1881.

S11. Pimblott, S., M.; LaVerne, J. A. Molecular Product Formation in the Electron Radiolysis of Water. *Radiation Research* **1992**, *129*, 265–271.

S12. Joseph, J. M.; Seon Choi, B.; Yakabuskie, P.; Clara Wren, J. A Combined Experimental and Model Analysis on the Effect of pH and O2(aq) on Γ-radiolytically Produced H2 and H2O2. *Radiation Physics and Chemistry* **2008**, *77*, 1009–1020.

S13. Yuk, J. M.; Park, J.; Ercius, P.; Kim, K.; Hellebusch, D. J.; Crommie, M. F.; Lee, J. Y.; Zettl, A.; Alivisatos, A. P. High-Resolution EM of Colloidal Nanocrystal Growth Using Graphene Liquid Cells. *Science* **2012**, *336*, 61–64.